INVESTIGATION OF THE STALLING CHARACTERISTICS OF A GENERAL AVIATION AIRCRAFT

Robert F. Stengel* and W. Barry Nixon**
Princeton University
Flight Research Laboratory
Department of Mechanical and Aerospace Engineering
Princeton, New Jersey, U.S.A.

ABSTRACT

Analytical and numerical estimates of the stalling characteristics of a small, single-engine aircraft are compared with flight test results. Analyses include nonlinear simulation and linear stability-and-control evaluation using aerodynamic and thrust characteristics obtained from a full-scale test in the NASA Langley Research Center 30' x 60' Wind Tunnel as well as sub-scale model test data. Flight tests include pre-stall calibration runs, symmetric gradual stalls, and mildly accelerated stalls in the vertical plane. These tests tend to confirm predictions based upon wind tunnel results, and they indicate areas in which special care must be taken in collecting data for aerodynamic parameter identification.

NOMENCLATURE

AR	aspect ratio = b^2/S
ARA	Avionics Research Aircraft
b	wing span, m(ft)
C_D	drag coefficient = drag force/$\bar{q}S$
C_L	lift coefficient = lift force/$\bar{q}S$
C_m	pitching coefficient = pitching moment/$\bar{q}S\bar{c}$
C_X	axial force coefficient = axial force/$\bar{q}S$
C_Z	normal force coefficient = normal force/$\bar{q}S$
$\bar{c}$	reference length, m(ft)
c.g.	center of gravity
F	stability matrix
$\underline{f}$	dynamic vector
G	control matrix
GA	general aviation
g	gravitational acceleration, $m/s^2(fps^2)$
$H_{x,\delta}$	output matrices
h_{cg}	axial c.g. location, %
I_{yy}	pitching moment of inertia, $kg\text{-}m^2$ $(slug\text{-}ft^2)$
i_t	tail incidence angle, deg
$i_{w_{r,t}}$	wing incidence angle, root and tip, deg
j	$\sqrt{-1}$
KIAS	knots indicated airspeed
$k_{1,2}$	altitude-hold control gains
l_t	distance between wing and horizontal tail centers of pressure, m(ft)
m	mass, kg (slugs)
m.a.c.	mean aerodynamic chord, m(ft)
P_{MAX}	maximum power available
PDM	pulse-duration modulation
q	pitching angular velocity, deg/s
$\bar{q}$	dynamic pressure = $\rho V^2/2$, $N/m^2(lb/ft^2)$
rpm	revolutions per minute
S	wing (reference) area, $m^2(ft^2)$
S_t	horizontal tail area, $m^2(ft^2)$
SL	sea level
T_c	thrust coefficient = thrust force/$\bar{q}S$
u	axial velocity, m/s(fps)
V	total velocity (airspeed), m/s(fps)
w	normal velocity, m/s (fps)
x	range, or aircraft axial position, m(ft)
$\underline{x}$	state vector
$\underline{y}$	output vector
z	altitude(negative), or aircraft normal position, m(ft)
α	angle of attack, deg
β	sideslip angle, deg
γ	flight path angle, deg
$\underline{\delta}$	control vector
δE	elevator angle, deg
δT	fraction of power available
η_p	propeller efficiency
θ	pitching angle, deg
λ	wing taper ratio = tip chord/root chord
ρ	air density, $kg/m^3(slugs/ft^3)$
σ	real part of eigenvalue
ω	imaginary part of eigenvalue
$\Delta(\ )$	perturbation quantity
$(\ )^*$	equilibrium value
$(\hat{\cdot})$	$(\cdot)\bar{c}/ZV$

INTRODUCTION

When an aircraft's angle of attack† is small, the lift produced by the wing and horizontal tail is proportional to that angle, facilitating flight path management through angular control. At sufficiently high angle of attack, the aircraft "stalls", i.e., the lift reaches a maximum value, and the ability to affect the flight path through angular control is greatly diminished. The resulting loss of lift, which often is accompanied by degraded lateral-directional control, creates a threat to safe flight that is especially critical at low altitude. On reaching the stall, the aircraft may develop a high sink rate or roll off into a spin. If the pilot fails to execute proper recovery procedures or has insufficient altitude within which to perform the recovery maneuver, ground impact is unavoidable.

The problem of stall/spin accidents is particularly severe for small light planes, or general

* Associate Professor of Mechanical and Aerospace Engineering.

** Senior Technical Staff Member and Chief Pilot.

† The aircraft's angle of attack is the angle (in the aircraft's vertical plane) between some datum line fixed to the aircraft, e.g., the centerline of the fuselage, and the aircraft's air-relative velocity vector.

aviation (GA) aircraft. In recent years (1965-1976), more than a tenth of all single-engine light plane accidents and nearly a third of all fatal light plane accidents in the United States have been related to the stall (Ref. 1 and 2). The problem predates man's first powered flight by several years -- aviation pioneer Otto Lilienthal was killed when his glider stalled in 1896 -- and it has been the subject of much research in the interim (Ref. 3). Nevertheless, much work remains to be done.

Early work on the stall by the British Aeronautical Research Committee included flight tests of biplanes to determine lateral-directional behavior in stalled flight (Ref. 4 to 6) and analyses of longitudinal stability at high angle of attack (Ref. 7 and 8). General observations on the stall were offered in Ref. 9, while Ref. 10 to 13 provide extensive material on stall aerodynamics for a variety of aircraft and wing planforms over a wide range of flight conditions. Computational simulations have augmented flight test, aerodynamic, and analytical results, as in Ref. 14 and several papers in Ref. 15, while Ref. 16 has treated the "superstall" case, for which the aircraft may possess multiple trim points at a single elevator setting. (Superstall normally is associated with swept-wing aircraft and "T" tails, but the "pitchup" characteristic that leads to the condition is not uncommon. Although the GA aircraft investigated below evidences the pitchup, with normal center-of-gravity locations it cannot trim in the superstall, as a consequence of control authority limits.)

Determining a full-scale aircraft's aerodynamic coefficients from flight data is a fundamental objective of flight testing. It is difficult to measure these data at high angles of attack because the coefficients often are nonlinear functions of the flight variables, and instrumentation is subject to increased error. In the past, stall testing has emphasized the measurement of static coefficients, flight variables, and control settings (Ref. 17 and 18); now, modern methods of parameter identification promise to yield dynamic coefficients (or derivatives) as well (Ref. 19 to 23). The latter techniques estimate parameters of given coefficient models with minimal error, and they can identify which model structure, in a set of candidate structures, provides the best fit to the data. However, these methods do not (at present) specify the candidate structures. If the model is inappropriate or incomplete, "best fit" coefficients that are physically illogical can be computed, as discussed in Ref. 20 and 24. Therefore, it is necessary to invoke additional knowledge, e.g., aerodynamic theory and wind tunnel testing, to formulate suitable structures for aerodynamic coefficient models.

The present investigation has been undertaken as a preliminary step in the development of new techniques for identifying stalling regime coefficients from flight test data. In this first stage, a comprehensive longitudinal aerodynamic model is developed from wind tunnel data, stalling maneuvers are simulated via digital computation, and the results are compared with the actual stalling maneuvers of a full-scale aircraft, Princeton's Avionics Research Aircraft (ARA). The ARA is well-suited for this study because full-scale wind tunnel data are available for angles of attack in the neighborhood of stall (Ref. 25 and 26). These static coefficients are augmented by full-scale dynamic derivatives measured in previous low-angle flight tests and by sub-scale data in the post-stall region. Quantitative results are complemented by photographs of smoke streams and surface-mounted thread tufts throughout the angle range.

Avionics Research Aircraft

Although the dimensions and aerodynamic characteristics of the ARA (Fig. 1a) are representative of current single-engine GA aircraft, the ARA has a number of features not found in production aircraft, including a five-degree-of-freedom variable-stability system which provides closed-loop, "fly-by-wire" control. The numerous sensors of this system provide data which can be recorded and processed for flight evaluation. Physical characteristics of the aircraft are similar to the standard Navion (Ref. 26) and are summarized in Table 1. The principal difference between the ARA and the Navion A is that the vertical tail and rudder have been lengthened by 0.36 m(14 in) for increased directional stability. The vertical fin has a 3° offset to counter thrusting effects. The table indicates that there is a 3° "washout" and increased camber in progressing from the wing root to tip, both of which encourage the root to stall before the tip, improving lateral controllability at high angles of attack. There are stall strips on the root leading edges to further promote root stall; the left strip is 0.56 m(22 in) long, and the right strip is 0.3 m(10 in) longer. The inertial characteristics represent the ARA with flight test instrumentation, single pilot, and 50% fuel loading. The aircraft was 54.4 kg (120 lb) heavier than the tabulated value at the beginning of a flight, and its c.g. was 0.35% aft of the reference value. These variations are ignored in the flight path simulations that follow.

The ARA's variable-stability system was not employed for the stalling tests, although the flap circuit was engaged to hold the flaps at zero deflection. The landing gear was locked down and the engine cowl flaps remained open during the tests.

Instrumentation for the stalling tests included linear accelerometers, attitude and rate gyros, angle-of-attack (α) and sideslip-angle (β) vanes, airspeed sensor, and control position potentiometers. In addition to these telemetered signals, the pilot reported panel readings of barometric altitude, airspeed, air temperature, and engine manifold pressure at regular intervals. The α and β vanes were mounted on streamlined housings that extended 0.71 m(2.33ft) laterally from the wingtip 35% chord stations. Angle-of-attack signals from opposite wing tips were summed to cancel roll rate effects, and the instruments were reset to allow a signal range of 0° to 52°. Inertial sensors were mounted within a few inches of the aircraft's c.g. Separate airspeed sensors, using the same stagnation port but different static ports, provided telemetered and cockpit data.

a) Avionics Research Aircraft.

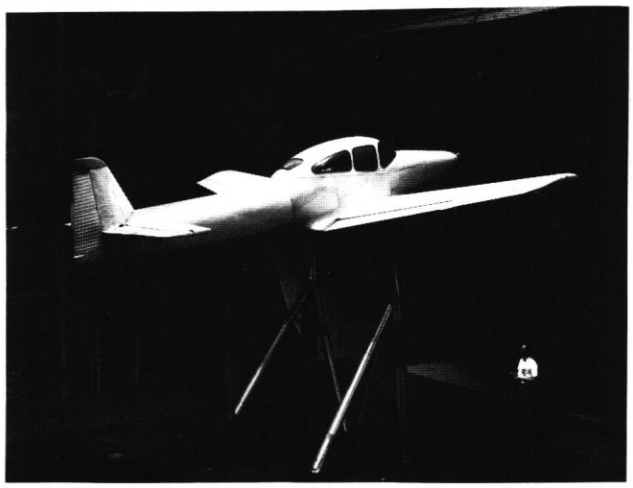

b) Full-Scale Wind Tunnel Test Vehicle

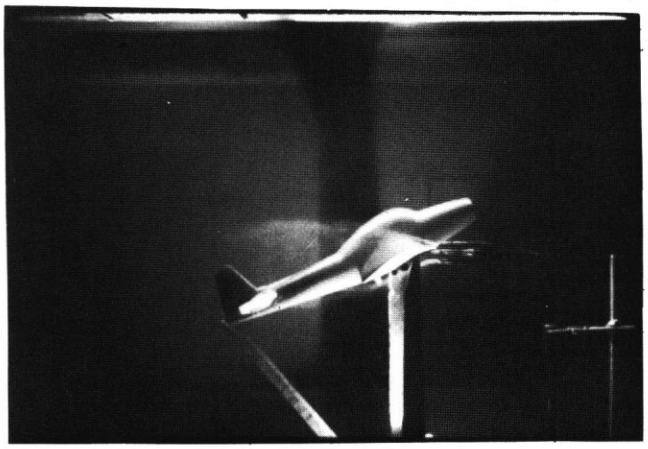

c) Sub-Scale Wind Tunnel Model

FIGURE 1. Test Vehicles and Model.

The ARA is equipped with a 212-kW(285-hp) reciprocating engine and rpm governor. Its 2.13 m (7 ft) propeller has two blades. Engine speed was regulated at 2300 rpm for these tests.

Full-Scale Wind Tunnel Airframe

The Navion airframe tested in the NASA Langley Research Center 30' x 60' Wind Tunnel (Fig. 1b) was standard in most respects. Horizontal tail incidences of ±5° were used in the wind tunnel tests. The reciprocating engine was replaced by a 198-kW(266-hp) electric motor with controllable pitch propeller (Ref. 25), allowing power effects for thrust coefficients, T_c', up to 0.23 to be assessed. The airframe was mounted on a three-point balance for force and moment measurements. Reference area and chord length of 16.72 m^2 (180 ft^2) and 1.73 m(5.67 ft), respectively, were used in reporting the data of Ref. 25 and have been adopted for the remainder of this report.

TABLE 1

Physical Characteristics of the Avionics Research Aircraft as Configured for Stall Testing

Wing
- Span, b, = 10.17 m(33.38 ft)
- Area, S, = 17.09 m^2(184 ft^2)
- Aspect Ratio, AR, = 6.04
- Taper Ratio, λ, = 0.54
- Root Incidence, i_{w_r}, = 2°
- Tip Incidence, i_{w_t}, = -1°
- Root Airfoil: NACA 4415R
- Tip Airfoil: NACA 6410R
- Mean Aerodynamic Chord, m.a.c. = 1.74 m(5.7 ft)

Horizontal Tail
- Tail Length, $\bar{l}_t$, = 4.72 m(15.5 ft)
- Area, S_t, = 3.99 m^2(43 ft^2)
- Incidence, i_t, = -3°
- Airfoil: NACA 0012
- Elevator Limits = +20° (trailing edge down), -30°

Inertial Characteristics
- Mass = 1203.85 kg(82.42 slugs)
- Pitch Inertia = 3396.57 kg-m^2(2503.12 slug-ft^2)
- Center of Gravity = 23.85% m.a.c. (25% m.a.c. located at 2.52 m(99.25 in) from datum)

Sub-Scale Wind Tunnel Model

The unpowered 1:16.7-scale model (Fig. 1c) is geometrically identical to the full-scale Navion. Ailerons, elevator, and flaps are movable; the vertical fin offset, tail incidence, wing washout, and chord section of the full-scale aircraft are duplicated. A 0.6 cm (0.25 in) strip of fine grit was applied to the upper wing surface at the 10% local chord as a boundary layer trip. The model was tested in Princeton's 2' x 3' Student Wind Tunnel and 3' x 4' 3-D Smoke Tunnel.

MATHEMATICAL MODEL OF THE AIRCRAFT

Force and Moment Coefficients

Full-scale lift, drag, and pitching moment coefficients were measured at angles of attack, α, ranging from -4° to 22° (Ref. 25). Measurements were made with the propeller removed and with idle to climbing thrust. Tunnel airspeed was 28.3 m/s (93 fps), giving a Reynolds number of 3.37 x 10^6.

The data presented in Ref. 25 were interpolated to provide values of C_L, C_D, and C_m for $i_t = -3°$ and for $T_c' = 0$, 0.12, and 0.23 throughout the α range. Elevator pitching effectiveness, $C_{m_{\delta E}}$, was obtained for $T_c' = 0$ and 0.23, while the corresponding effect on normal force was represented by $C_{Z_{\delta E}} = C_{m_{\delta E}} (\bar{c}/\bar{l}_t)$. In this study, $C_{m_{\delta E}}$ was assumed to remain constant up to $\alpha = 45°$, at which point it decreased as sin 2α, in accordance with a Newtonian approximation for the flow over the tail.

The static coefficients, together with their body-axis transformations, C_X and C_Z, exhibit conventional variations with α (Fig. 2): C_L is linear in α, C_D is quadratic in α, and C_m (measured about the 25% mean aerodynamic chord, m.a.c.) decreases in stable fashion. The zero-lift C_m is large, leading to strongly positive (trailing edge down) values of elevator deflection, δE, for trim. (Although not shown, $C_{m_{\delta E}}$ ranges from -0.018 to -0.022 per deg with power off and -0.127 to -0.034 per deg with $T_c' = 0.23$ in the measured α range.) C_L and C_D represent net nondimensional force-balance measurements, i.e., thrust and aerodynamic effects are not separated; hence, C_D takes on negative values as the thrust increases. C_L is augmented by thrust at all α because the air velocity over the wing's inboard section is increased in the propeller's wake. Zero-thrust lift appears to reach its maximum (stalled) value at $\alpha = 22°$; thrust decreases α_{STALL}, but $C_{L_{MAX}}$ increases by 16%, due, in part, to tilting of the thrust axis. Because ARA flight tests were made with the cowl flaps open and landing gear down, an increment of 0.006 was added to the values of C_D shown in Fig.2.

Dynamic derivatives were not measured in the full-scale tunnel tests, so estimates were based upon the flight test results of Ref. 24. These maximum-likelihood parameter estimates used flight data from the Variable-Response Research Aircraft (VRA), which was dynamically identical to the ARA at the time of the tests. (Side-force panels have since been mounted on the VRA's wings. The panels have little effect on the aircraft's longitudinal dynamics but markedly alter lateral-directional stability and control.) Lacking measurements for varying α and T_c', constant values of -18.1, -15.9, and -6.5 per rad were used for $C_{m_{\hat{q}}}$, $C_{z_{\hat{q}}}$, and $C_{m_{\dot{\hat{\alpha}}}}$, respectively.

The static aerodynamic coefficient tables were extended to $\alpha = 60°$ using sub-scale wind tunnel data contained in a university senior's project report (Ref. 27). Student wind tunnel airspeed was 40 m/s(130 fps), with an equivalent Reynolds number of 2.8×10^5. At low α, the unpowered full-scale and sub-scale C_L differed by a maximum of 10%; trends in the sub-scale C_D and C_m were in agreement with the full-scale data and were within 10% of full-scale numerical values at $\alpha = 22°$. The sub-scale data taken at higher angles was appended to the full-scale data, with approximate bias corrections for the differences in sub- and full-scale values in the 18°-to-22° α range but without tunnel wall or blockage corrections. Power was assumed to have the same incremental effects on C_X and C_Z as on the full-scale airframe at $\alpha = 18°$ to 22°; power effects on C_m at high α were neglected.

The combined zero-thrust static longitudinal coefficients, illustrated in Fig. 3, have three characteristics of note. The wing stalling effects are confined principally to C_L, which shows a pre-stall flattening at $\alpha = 18°$ and a stall break at $\alpha = 22°$. C_D is quadratic in α for low angles, but it is linear in the 20°-to-50° range. The pitching moment slope changes sign for $\alpha = 38°$ to 45°, implying a region of local instability and the possibility of a superstall equilibrium beyond $\alpha = 45°$; however, neither problem can occur unless the aircraft can trim in the region. With the rotational center at 25% m.a.c. (as shown), the maximum ΔC_m that can be produced by the elevator is 0.54, far short of the 0.9 required for trim at high α. An aft center-of-gravity (c.g.) shift of more than 20% would be required to experience pitch instability or superstall with full negative δE; this would place the c.g. well behind its certified aft limit.

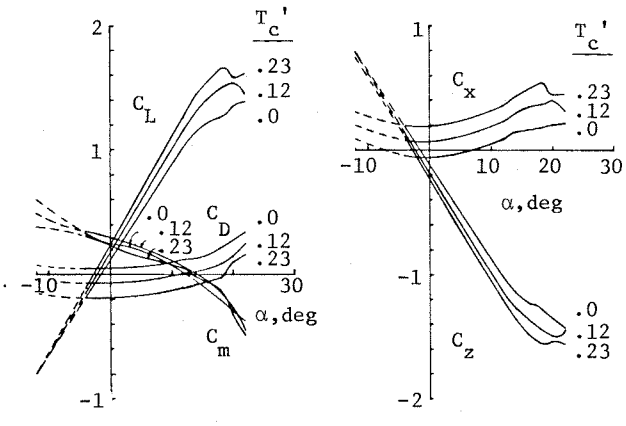

FIGURE 2. Static Longitudinal Coefficients from Full-Scale Wind Tunnel Tests.

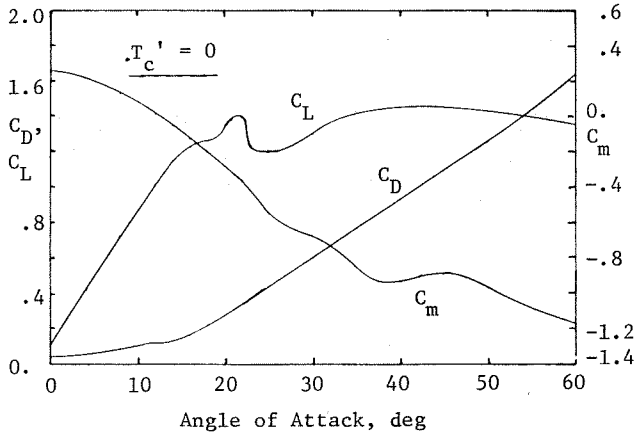

FIGURE 3. Combined Static Longitudinal Model (zero thrust).

Results of Flow Visualization

Insight regarding the flow which leads to the forces and moments shown in Fig. 3 was gained using two flow visualization techniques. Thread tufts were glued to the sub-scale model's upper surfaces, fuselage, and vertical tail for tests at 40 m/s in the Student Wind Tunnel. Photographs of air flow adjacent to the sub-scale model were taken with stream velocities of 3 to 5 m/s (10 to 16 fps) in the 3-D Smoke Tunnel.

Both techniques showed an area of flow separation on the upper wing surface near the root trailing edge with $\alpha = 0°$. The separated flow progressed forward and outward as angle of attack increased, and an area of separated flow appeared in the vicinity of the flap-aileron juncture, which, with the hingelines, was taped for the tests. Figure 4 illustrates the tuft pattern when $\alpha = 13.5°$.

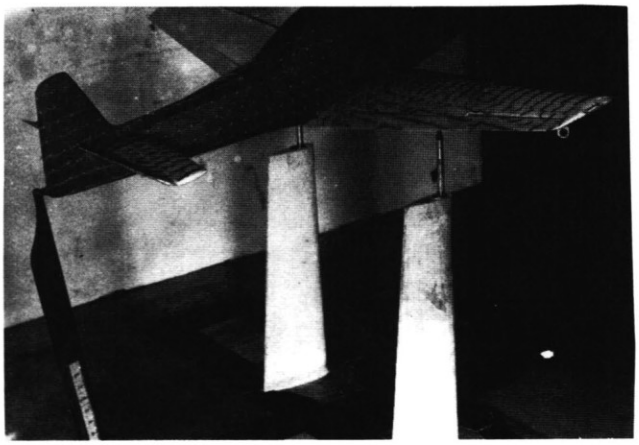

FIGURE 4. Tuft Pattern for $\alpha = 13.5°$.

The horizontal tail is immersed in the wing wake up to angles well beyond the stall. Spanwise deflection of the wake is negligible at all angles; wing incidence and high camber provide zero-α lift, and tip vorticity is present at angles of zero and above. The stall break is characterized by increasingly diffuse wing wake and tip vortex. At $\alpha = 20°$, the flow at mid-span is fully separated but fairly straight past the wing (Fig. 5a); at $\alpha = 25°$, the leeward flow billows (Fig. 5b). The tip vortex has a well-defined core at the lower angle (Fig. 6a) that becomes diffuse at the higher angle (Fig. 6b). (Figure 1c shows the flow near the wing root at $\alpha = 25°$.)

The horizontal tail emerges from the central portion of the wing wake in the vicinity of the "unstable" pitching moment break, i.e., at angles near 40°. The wing produces less downwash as α increases, and the wing and tail flow fields are essentially independent when $\alpha = 60°$ (Fig. 7). The figure illustrates that streamlines immediately adjacent to the wing clear the tail (Fig. 7a); that streamlines pass entirely between the wing and tail (Fig. 7b); and that streamlines impinging on the tail experience very little wing-induced downwash (Fig. 7c).

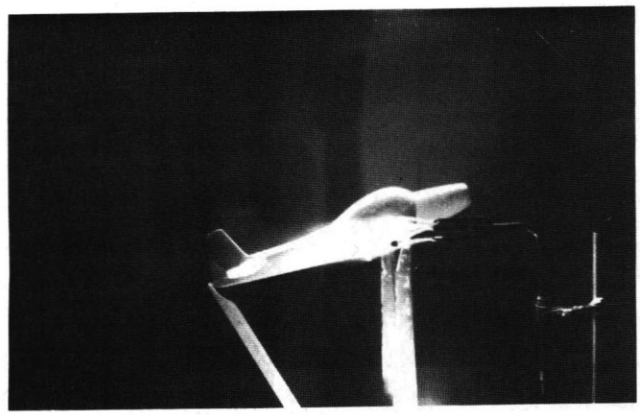

a) $\alpha = 20°$

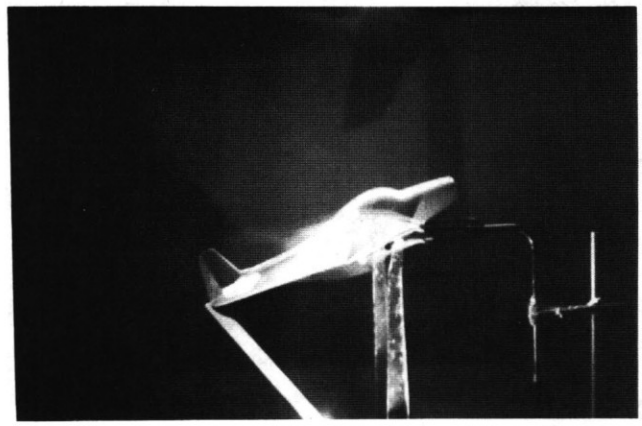

b) $\alpha = 25°$

FIGURE 5. Mid-Span Flow.

Thrust Model

The ARA's thrust model is a complex function of power available, rpm, throttle setting, and propeller efficiency which must be related to the thrust coefficient (T_c') in order to determine C_L, C_D, and C_m (as in Fig. 2). A detailed description is beyond the scope of this paper, but the development, which follows Ref. 28, takes account of the fact that the ARA is equipped with a variable-pitch, constant-rpm propeller. At a fixed altitude, a constant-rpm reciprocating engine operates at constant power, and the thrust delivered by the propeller is simply power divided by velocity. The power delivered, accounting for propeller efficiency (in turn a function of the propeller's advance ratio), is a function of altitude. The control variable, δT, varies between 0 and 1, modulating the power available, and, therefore, the thrust. Since thrust = $T_c' \bar{q} S$ and the dynamic pressure, $\bar{q}$, is determined by the flight condition, δT specifies T_c'. δT approximates a sine function of the cockpit throttle quadrant setting.

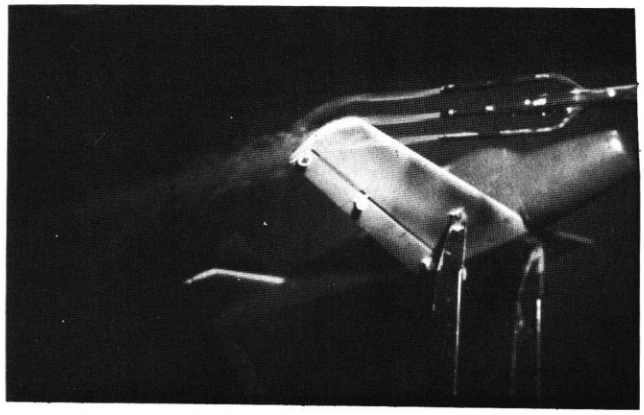

a) α = 20°

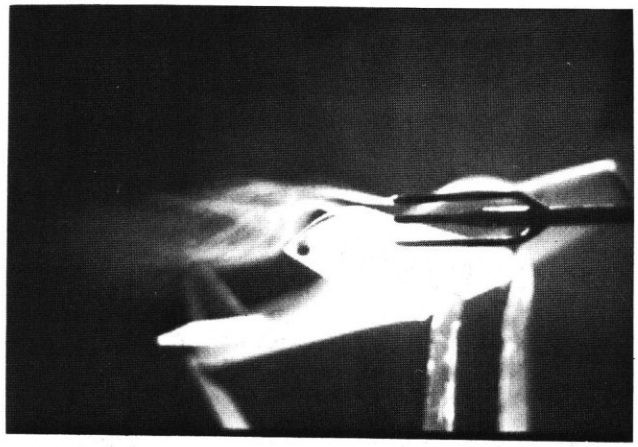

b) α = 25°

FIGURE 6. Wing Tip Flow.

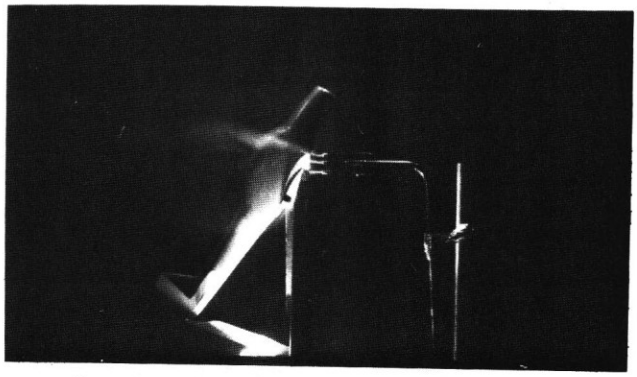

a) Wing Flow

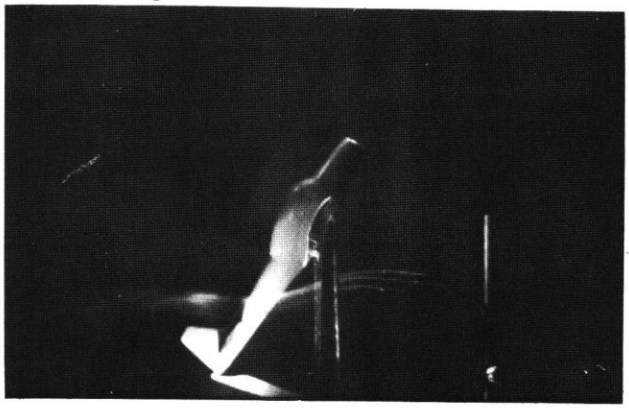

b) Flow between Wing and Tail

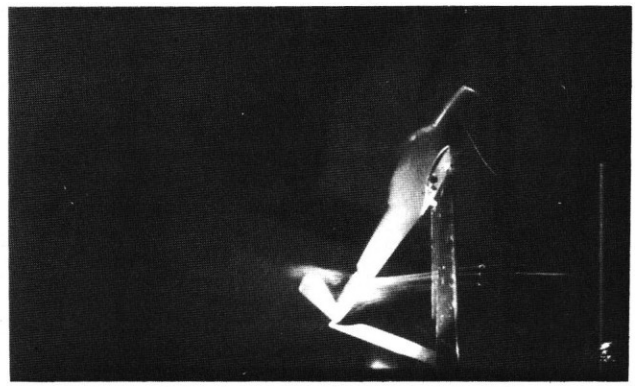

c) Horizontal Tail Flow

FIGURE 7. Smoke Streams for α = 60°.

COMPUTATIONAL ANALYSIS

Longitudinal Equations of Motion

ARA flight paths were simulated by numerically integrating six ordinary differential equations:

$$\dot{u} = [C_X(\alpha,T_c') - C_{D_G}\cos\alpha]\bar{q}S/m - g\sin\theta - qw \quad (1)$$

$$\dot{w} = C_{Z_T}\bar{q}S/m + g\cos\theta + qu \quad (2)$$

$$\dot{q} = \{[C_m(\alpha,T_c') + C_{Z_T}\Delta h_{cg} + C_{m_{\hat{q}}}(\frac{q\bar{c}}{2V}) + C_{m_{\delta E}}(\alpha,T_c')(1 + \frac{\Delta h_{cg}\bar{c}}{l_t})\delta E]V^2 + C_{m_{\hat{\dot{\alpha}}}}\dot{w}/2\}\rho S\bar{c}/2I_{yy} \quad (3)$$

$$\dot{\theta} = q \quad (4)$$

$$\dot{x} = u\cos\theta - w\sin\theta \quad (5)$$

$$\dot{z} = -u\sin\theta + w\cos\theta \quad (6)$$

where

$$\alpha = \tan^{-1}(w/u) \quad (7)$$

$$V = (u^2 + w^2)^{1/2} \quad (8)$$

$$\bar{q} = \rho V^2/2 \quad (9)$$

$$\rho = \rho_{SL}e^{(3.525 \times 10^{-5})z(ft)} \quad (10)$$

$$C_{Z_T} = C_Z(\alpha,T_c') + C_{Z_{\hat{q}}}(\frac{q\bar{c}}{2V}) + C_{Z_{\delta E}}(\alpha,T_c')\delta E - C_{D_G}\sin\alpha \quad (11)$$

$$T_c' = 2\eta_p P_{MAX}\delta T/\rho_{SL}SV^3 \quad (12)$$

Δh_{cg} represents any shift of the c.g. from the reference point as a fraction of m.a.c. C_{D_G} is the drag coefficient of the gear and cowl flaps. In eq. 3, angle-of-attack-rate damping is assumed proportional to $\dot{w}$, which is given by eq. 2.

Linear interpolation of tabulated data and fourth-order Runge-Kutta integration were used in the solution of these equations.

Equations 1 to 6 can be expressed as the state equation

$$\dot{\underline{x}} = \underline{f}(\underline{x},\underline{\delta}) \tag{13}$$

The state vector, $\underline{x}$, contains body-axis axial and normal velocities (u,w), pitch rate (q), pitch angle (θ), and inertial forward and vertical position (x,z). The control vector, $\underline{\delta}$, contains elevator angle (δE) and power control (δT). Given airspeed, altitude, and aircraft configuration, level flight trim values of α, δE, and δT were found by minimizing a quadratic function of $\dot{u}$, $\dot{w}$, and $\dot{q}$. At a function minimum, the three rates are zero, $q = 0$, and $\theta = \alpha$.

Linearized equations of motion, useful for assessing the stability of the aircraft and its response to small perturbations, are found by expanding both sides of eq. 13 in Taylor series. The trim condition specifies the nominal (zeroth-order) solution, while the perturbation equations are specified by the first-order terms of the expansion:

$$\Delta\dot{\underline{x}} = F\Delta\underline{x} + G\Delta\underline{\delta} \tag{14}$$

with

$$F = \partial\underline{f}/\partial\underline{x}\,\Big|_{\substack{\underline{x}=\underline{x}_o \\ \underline{\delta}=\underline{\delta}_o}} \quad , \quad G = \partial\underline{f}/\partial\underline{\delta}\,\Big|_{\substack{\underline{x}=\underline{x}_o \\ \underline{\delta}=\underline{\delta}_o}} \tag{15,16}$$

F and G contain the conventional stability-and-control derivatives; they can be approximated at each trim point by $\Delta\underline{f}/\Delta\underline{x}$ and $\Delta\underline{f}/\Delta\underline{\delta}$, respectively i.e., by repeated evaluation of eq. 13 with incremental variations in the state and control. The local stability of flight path motions then is predicted by the eigenvalues of F, while the relative involvement of the state components in each mode of motion is predicted by the associated eigenvectors (Ref. 29).

Equilibrium solutions of eq. 14 are found by setting $\Delta\dot{\underline{x}} = 0$; denoting steady-state values by $(\,)^*$,

$$\Delta\underline{x}^* = -F^{-1}G\Delta\underline{\delta}^* \tag{17}$$

The equation describes the aircraft's response to the pilot's commands after all transients have decayed; as such, it is a fundamental measure of aircraft behavior.

Conversely, the control perturbations required to cause a given variation in trim condition can be found by solving eq. (17) subject to an auxiliary constraint,

$$\Delta\underline{y}^* = H_x\Delta\underline{x}^* + H_\delta\Delta\underline{\delta}^* \tag{18}$$

as in Ref. 30. The two equations are solved simultaneously to find both state and control perturbations corresponding to the desired trim variation, $\Delta\underline{y}^*$:

$$\begin{bmatrix} \Delta\underline{x}^* \\ \Delta\underline{\delta}^* \end{bmatrix} = \begin{bmatrix} F & G \\ H_x & H_\delta \end{bmatrix}^{-1} \begin{bmatrix} 0 \\ \Delta\underline{y}^* \end{bmatrix} \tag{19}$$

Because eq. 13 is sixth-order, eq. 14 is sixth-order. The six eigenvalues represent the aircraft's short period, phugoid, height, and range modes. Range (x) does not alter the "flat-earth" dynamics of eq. 1 to 6, so its eigenvalue is identically zero, and the remaining five eigenvalues can be determined without consideration of range.

The height mode (Ref. 31) arises from the altitude dependency of air density. The ARA's height mode has a stable time constant of about 1000 sec, substantially longer than the time scales of the short period and phugoid modes and of no direct consequence in the evolution of the stall. The short period "attitude" mode and phugoid "energy" mode are well described by a fourth-order model using Δu, Δw, Δq, and $\Delta\theta$ as state variables. There is, however, an important difference between the equilibrium solutions of fourth- and fifth-order models: the former admits steady-state solutions with non-zero flight path angle, i.e., steadily changing altitude, whereas the latter does not. In the first case, a thrust increase leads to a steady climb; in the second, the climb angle diminishes with decreasing air density. The fourth-order trim solution is seen to be only quasi-steady, but for time scales shorter than the height mode time constant, it provides useful results.

Quasi-steady trim values of true airspeed, V, and flight path angle, γ, are central to flight path management, and any effects which stall may have on the relationships between ΔV^*, $\Delta\gamma^*$, and control perturbations are of interest. Expanding eq. (7) and (8) and noting that

$$\gamma = \theta - \alpha \tag{20}$$

in planar motion, $\Delta\underline{y}^* = [\Delta V^* \Delta\gamma^*]^T$, and

$$\Delta V^* = (u_o\Delta u^* + w_o\Delta w^*)/V_o \tag{21}$$

$$\Delta\gamma^* = \Delta\theta^* + (w_o\Delta u^* - u_o\Delta w^*)/V_o^2 \tag{22}$$

This specifies H_x for eq. (19). As the control enters neither equation, $H_\delta = 0$.

Trim and Stability Characteristics

Trim characteristics with the nominal weight and center of gravity are estimated as functions of airspeed in Fig. 8 using the wind tunnel data and the nonlinear equations of motion. At an altitude of 2286 m(7500 ft), maximum airspeed is 115 KIAS, and the minimum-power airspeed is 65 KIAS. The negative tail incidence leads to positive elevator settings, except at the lowest airspeeds, where high α is required for level flight. Flight measurements of trim, denoted by symbols in Fig. 8, are discussed in a later section.

Corresponding short period and phugoid eigenvalues (upper half-plane only) are plotted in

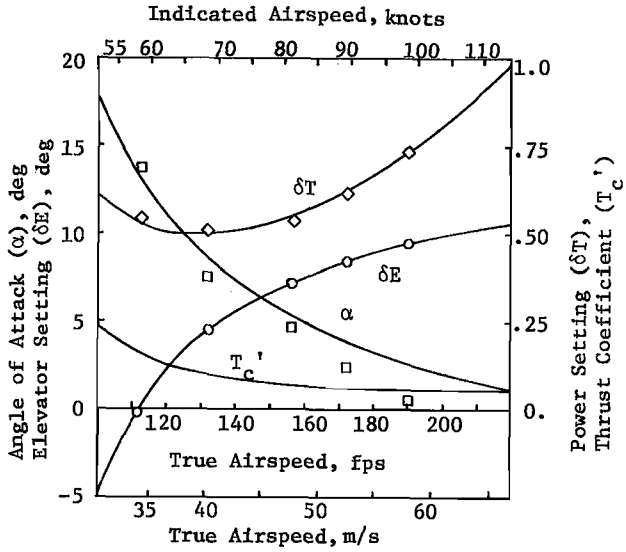

FIGURE 8. Trim Characteristics of the ARA. Altitude = 2286 m(7500 ft). Solid Lines Generated by Wind Tunnel Data; Flight Test Results Indicated by Symbols.

Fig. 9. Above the minimum-power point, increasing speed leads to higher short period natural frequency with modest increase in damping. Below this point, decreasing speed has little effect on natural frequency, but there is a sharp drop in short period damping as stalling angles are approached. Concurrently, the phugoid natural frequency increases, and there is more coupling between altitude and flight path variables. This is reflected in the magnitude of eigenvector components, illustrated by Fig. 10. The $\Delta\alpha$ and Δq components of the phugoid eigenvector are somewhat larger at low speed than at high speed, while Δu plays a greater part in short period motion at low speed than at high speed.

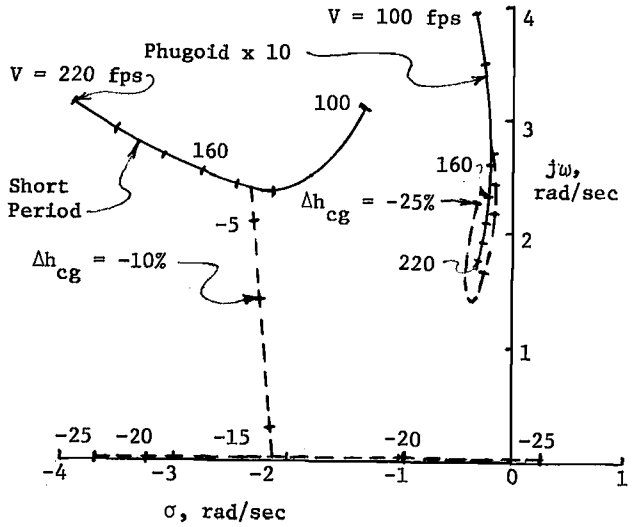

FIGURE 9. Effects of Trim Airspeed and c.g. Location on Short Period and Phugoid Eigenvalues. Altitude = 2286 m(7500 ft).

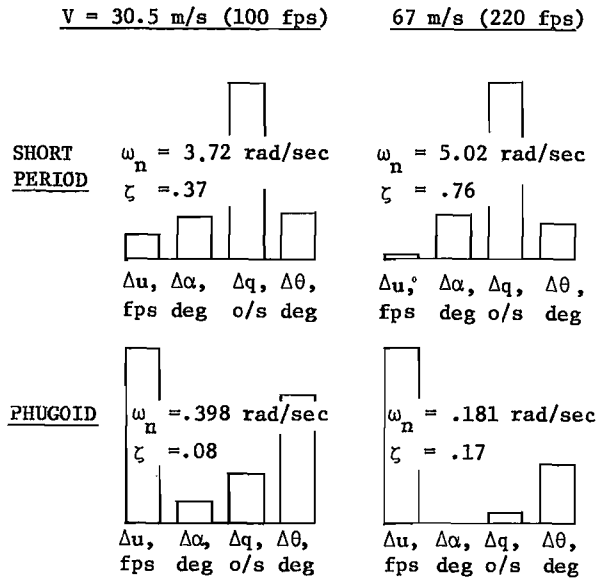

FIGURE 10. Eigenvector Magnitudes at Two Trim Airspeeds. Altitude = 2286 m(7500 ft).

Figure 9 also shows the destabilizing effect of aft c.g. travel for a velocity of 40.8 m/s (133.8 fps). The effect on phugoid roots is minimal, but the complex short period roots coalesce with an aft shift of 16%, and one root eventually becomes unstable.

Trim sensitivities also vary with airspeed. Using eq. 17, 21, and 22, Figure 11a presents $\Delta\gamma^*/\Delta\delta E^*$, $\Delta V^*/\Delta\delta E^*$, $\Delta\gamma^*/\Delta\delta T^*$, and $\Delta V^*/\Delta\delta T^*$ for the fourth-order linear model at the nominal altitude. Holding throttle constant, small positive perturbations of the elevator are shown to decrease the steady-state flight path angle above the minimum-power point, and they lead to increased velocity during the resulting descent. Small positive variations in throttle setting (with no elevator compensation) cause the aircraft to climb; for nominal trim speeds below 60 m/s (190 fps), the climb is accompanied by a small loss in airspeed.

The inverse relationships, found from eq. (19), (21), and (22) are plotted in Fig. 11b. Elevator and throttle settings required for unit changes in $\Delta\gamma^*$ and no change in ΔV^* are shown as solid lines, whereas control variations for ΔV^* variations without $\Delta\gamma^*$ variations are shown by dashed lines. To climb without changing airspeed when the nominal airspeed is above 32 m/s (105 fps), the throttle is advanced. The control yoke is pushed forward (positive $\Delta\delta E$) substantially at low speed, but there is negligible deflection for airspeeds above 40 m/s (~130 fps). Incremental changes in airspeed are accomplished primarily with the elevator, and the corresponding throttle correction changes sign at the minimum-power point.

Examples of Stalling Response

The aerodynamic model and equations of motion are used to simulate gradual and abrupt stalls and to demonstrate the superstall in the vertical plane. The abrupt ("accelerated") stall is readily

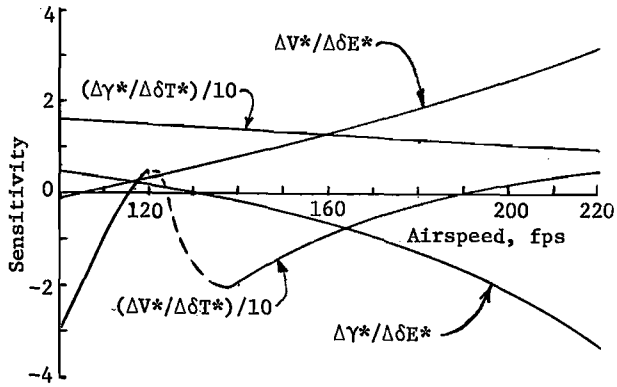

a) Effects of Control on Trim V and γ.

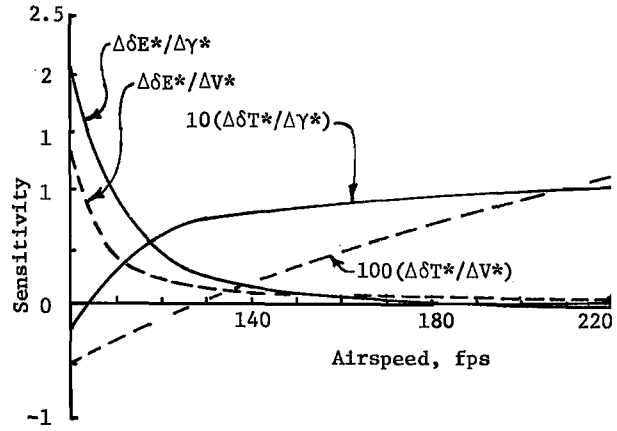

b) Control Settings Required for Independent Trim Perturbation.

FIGURE 11. Linear Trim Sensitivities as Functions of Airspeed. Altitude = 2286 m (7500 ft).

simulated using step changes in control settings, but the gradual stall can occur only as the result of smoothly changing control. To provide some common basis for computation and flight test, the gradual stall was entered as a consequence of attempting to hold altitude with elevator alone once the throttle had been retarded to idle. During the ARA flights, the pilot used the rate-of-climb indicator as his primary control reference, with occasional reference to the altimeter. For the computed simulation, an analogous closed-loop control law was implemented:

$$\delta E(t) = k_1[k_2\dot{z}(t) + z(t)] + \delta E_o \qquad (23)$$

δE_o was the trim elevator setting prior to thrust cutoff. Control gains of $k_1 = -.3$ and $k_2 = 5$ provided smooth stall entries at the nominal starting condition of 70 KIAS and 2286-m(7500 ft) altitude.

With zero thrust, the aircraft begins to descend, and the closed-loop elevator setting grows until the saturation limit is reached. Figure 12 compares a descent at the original trimmed elevator setting (Case A) with closed-loop flight paths (Cases B to D) in which the elevator limits at -10°, -20°, and -30°, respectively. Once the throttle is cut, Case A is characterized by a large-amplitude phugoid oscillation and rapid altitude loss at nearly constant α. The closed-loop controls keep altitude within 18 m(60 ft) of its original value for the first 10 sec; control saturation leads to retrimming at pre-stall (Case B), stall (Case C), and post-stall (Case D) angles of attack. Phugoid oscillations and rapid rates of descent follow in all three cases. Note that there is no particularly severe motion in passing through the stall (Case D), although the magnitudes of resulting motions are proportionately larger than for Cases B and C.

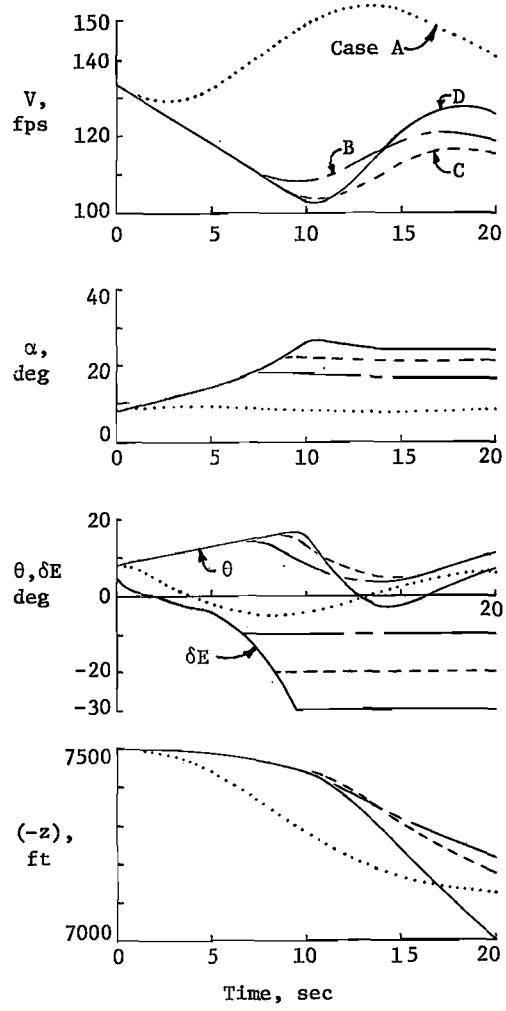

FIGURE 12. Power-off Flight Paths of the ARA with Initial Trim Elevator (Case A) and Altitude-Hold Elevator Control. Elevator Saturates at -10°(Case B), -20° (Case C), and -30°(Case D).

Figure 13 shows that the stability and mode shapes in the stalled region are somewhat similar to the unstalled case, but the quasi-steady trim perturbation behavior is decidedly different. To produce this figure, linear models for the four cases were generated at points near t = 15 sec characterized by unity load factor. Short-period eigenvalues of the pre-stall, stall, and post-stall cases have about the same natural frequency but less damping than the unstalled case, while phugoid eigenvalues evidence higher frequency and greater damping (Fig. 13a). The eigenvector magnitudes

indicate greater coupling between the modes in the stall regime, but not of an inordinate degree. (Fig. 13b). For all the cases, increasing $\Delta\gamma^*$ requires increased throttle and elevator (pitch down) settings, but the throttle requirement for velocity variations changes sign in the stall regime (Fig. 13c).

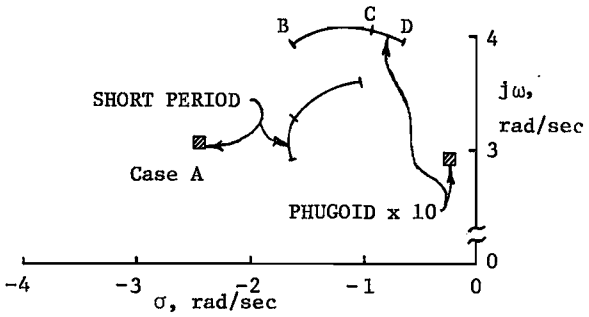

a) Eigenvalues

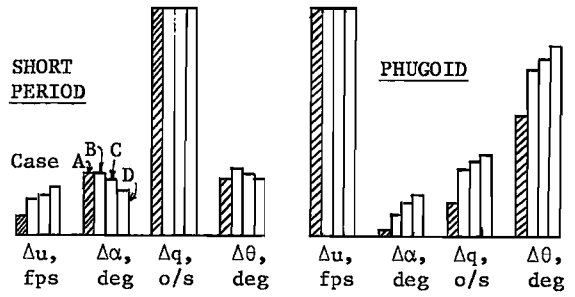

b) Eigenvector Magnitudes

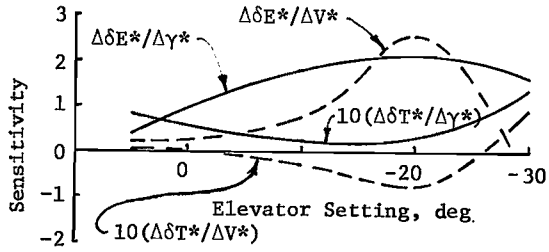

c) Trim Control Sensitivities

FIGURE 13. Survey of Stability-and-Control Characteristics for the Power-Off Flight Paths.

As suggested earlier, it is possible to trim in the superstall region if the c.g. is moved far enough aft. For the present model, the elevator limit also must be increased, because low-α static instability prevents Δh_{cg} from exceeding -22%. (See Fig. 3 for the nonlinearity in C_m that leads to this result.) Figure 14 illustrates the gradual stalls which occur with this aft c.g. position and elevator limits of -30°, -34°, and -34.5° (Cases A, B, and C). The altitude-hold elevator trace is similar to that experienced with forward c.g., but there is a 2-sec neutral oscillation in δE prior to its divergence to saturation. As before, α and V compensate for the lost thrust

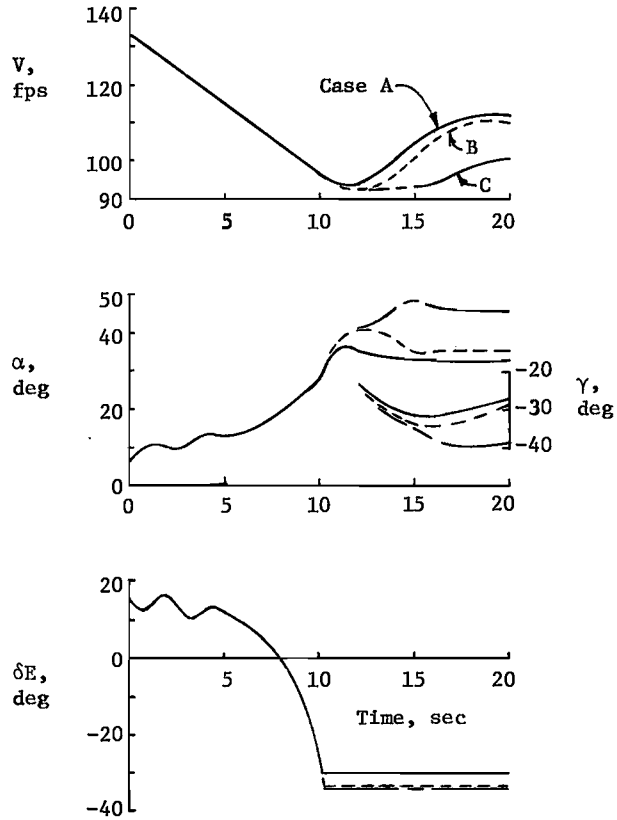

FIGURE 14. Effects of Aft c.g. and Varying Elevator Limits on Power-Off Flight Paths. $\Delta h_{cg} = -0.22$. Elevator Saturates at -30°(Case A),-34°(Case B), and -34.5° (Case C).

up to the elevator limit. The Case A angle-of-attack trace is similar to the forward c.g. results, although overshoot and quasi-steady values of α are larger. Case B shows greater overshoot before settling at an α slightly higher than Case A's.

Increasing the δE limit by one-half degree evokes a jump to the superstall angle of attack. The 3-sec transition from α = 41° to 49° is accompanied by a modest pitchup, and it results ultimately in descent at steeper flight path angle and lower airspeed. In the present case, recovery to lower α could be accomplished readily by positive deflection of the elevator.

Power setting can have a major influence on the abrupt stall, as Fig. 15 shows. Beginning at 90 KIAS and 2286-m(7500 ft) altitude, the elevator is deflected -16° from trim. For Case A, δT is unchanged; for Case B, δT is simultaneously zeroed. In both cases, the aircraft pitches up and loses airspeed. With power off, the aircraft begins to level off before α has reached its maximum, stalling value. With power on, the aircraft drives to higher γ and more nearly vertical pitch attitude (θ_{max} = 70°). Gravity has greater affect on airspeed, and as the aircraft falls through, the combination of low airspeed and high attitude momentarily drives angle of attack beyond 50°. The minimum pitch rate lags the maximum α, confirming the fact that the extreme flight path, and not

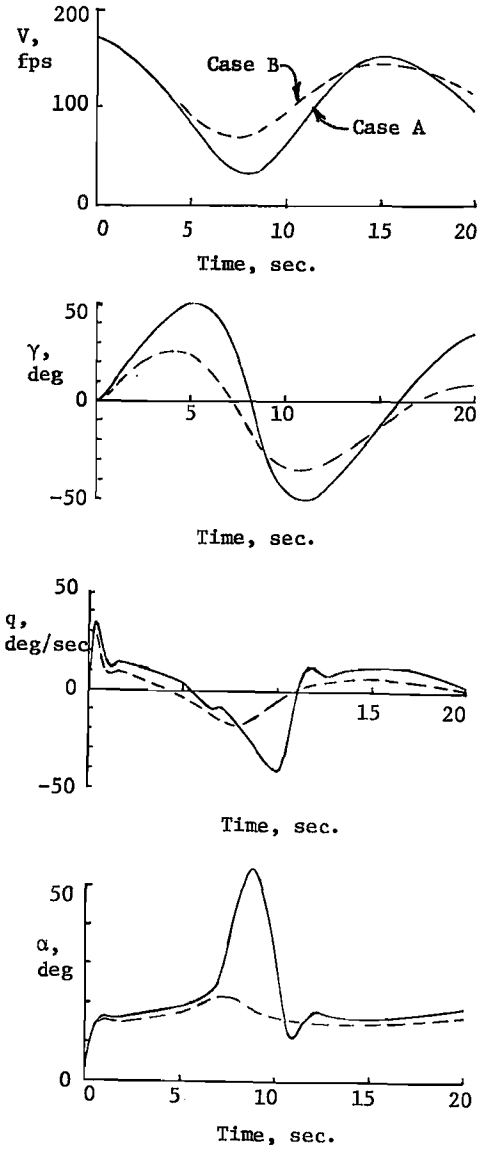

FIGURE 15. Effect of Power on the Abrupt Stall. Altitude = 2286 m(7500 ft).

attitude dynamics, is the source of the α excursion.

This section concludes with an example of what might be called "pseudo-stall", in which non-stalling flight motions during takeoff could deceive the novice pilot, with possibly severe consequences. Consider what happens when the aircraft is initially trimmed for 62 KIAS (105 fps) at sea level and the throttle is advanced from 35% (trim) to full power with no corresponding elevator correction. Figure 16 illustrates that α actually decreases as the aircraft begins to climb, but a large-amplitude phugoid oscillation is excited by the throttle advance. In 9 sec, θ has topped 30°, and velocity is decreasing. With no further control actions the aircraft will continue to climb, although γ drops near zero periodically. If the pilot mistakes high θ for high α or is momentarily distracted during the θ buildup, he may push the yoke forward just as the aircraft is about to correct for the out-of-trim condition. Flight path angle then is likely to drop below

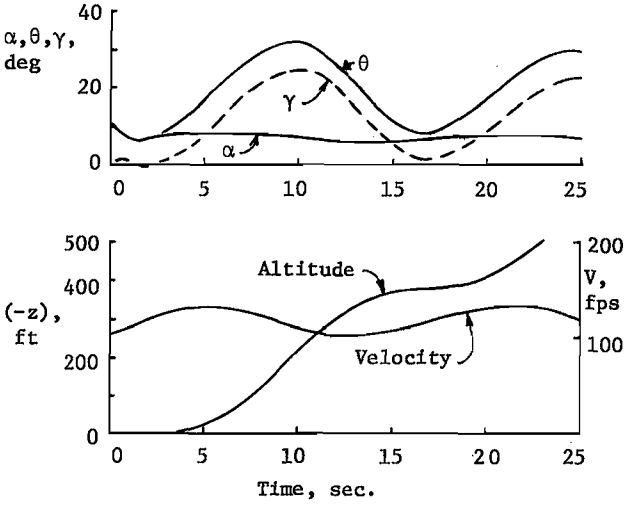

FIGURE 16. Phugoid Oscillation Caused by Advance to Full Power without Retrimming the Elevator. Altitude = Sea Level.

zero, and, since the aircraft is in close proximity to the ground, the possibility of collision with obstacles is increased. Figure 11b illustrates that the problem could be avoided by pushing the yoke forward as the throttle is advanced, which is standard piloting technique.

FLIGHT TEST RESULTS

Several ARA flights were conducted to provide a preliminary assessment of the operational problems associated with stall testing and to provide data with which the wind tunnel/computer results could be compared qualitatively. These flights set the stage for the nonlinear parameter identification to follow, which will use data from improved recording systems currently in development. Objectives of these flights included the determination of longitudinal trim characteristics, response to elevator doublets, gradual and abrupt stall behavior, and sensor calibrations.

Level-flight testing occurred at a pressure altitude of 2286 m(7500 ft), while stalls were initiated from an altitude of 2438 m(8000 ft). This provided smooth air for measurements, as well as sufficient altitude margin within which stalling motions could be examined and safe recovery could be effected. Air temperatures during testing were about 5°C above standard atmosphere values. Longitudinal and lateral-directional data were recorded using PDM radio telemetry and voice reporting.

Flight measurements of trim conditions were compared with computed predictions in Fig. 8. Elevator settings were virtually identical, but the divergence in α suggests a difference in the pitching moment sensitivity. Trim tabs were used to deflect the elevator in flight, but were assumed to be undeflected in the computed elevator trim setting. The flight values of percentage power available, δT, represent a linear regression of experimentally determined manifold pressure with computed results.

The pilot initiated ARA stall using the

altitude-hold technique described earlier, providing the flight path summarized by Fig. 17. Power was quickly retarded to the 30.5-cm (10-in) Hg manifold pressure idle point, which very nearly approximates zero thrust. The elevator history was similar to that of Fig. 12, but the pilot used higher gains than those assumed in eq. (23). As a consequence, the elevator stop was reached more quickly, and α and θ responses were more peaked. Light-to moderate buffet, corresponding to an rms pitch rate disturbance of 1/4 deg/sec, was experienced at α of 15° and above. This, combined with lateral-directional perturbations, is believed to be responsible for the occasional short-period oscillations that occur during the run. While it is possible that oscillations are due to a multivalued nonlinearity such as hysteresis, as described in Ref. 32, there are insufficient data on which to base such a conclusion.

The ARA stall was entered without significant rolling motion, but a 3-sec Dutch roll oscillation built up as the stall was maintained. The motion initially could be controlled within ±5° using rudder alone; if left unchecked, it increased to ±20° amplitude during an interval of half a minute, and aileron control was necessary to hold the wings nearly level.

Power-off recovery was affected by bringing the elevator back to a normal setting (Fig. 18).

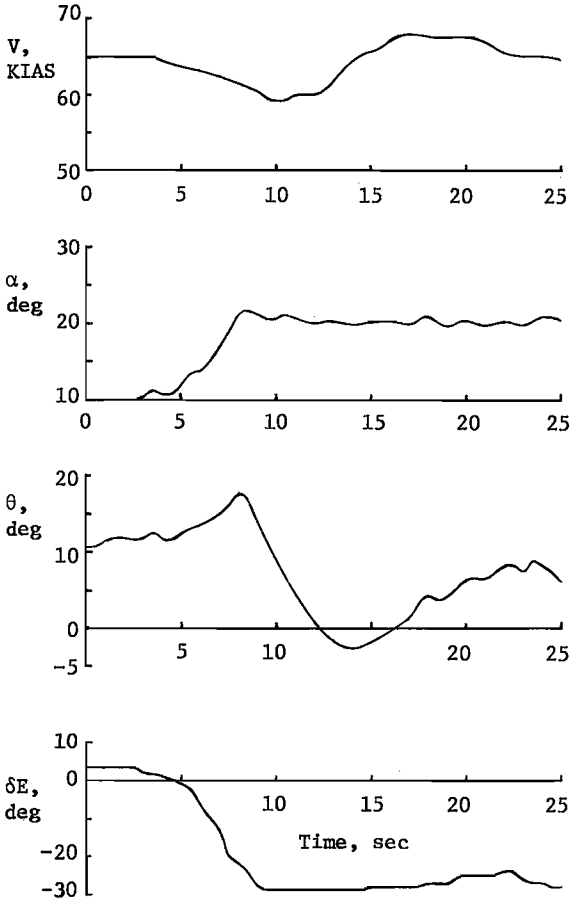

FIGURE 17. Gradual ARA Stall. Starting Altitude = 2438 m(8000 ft).

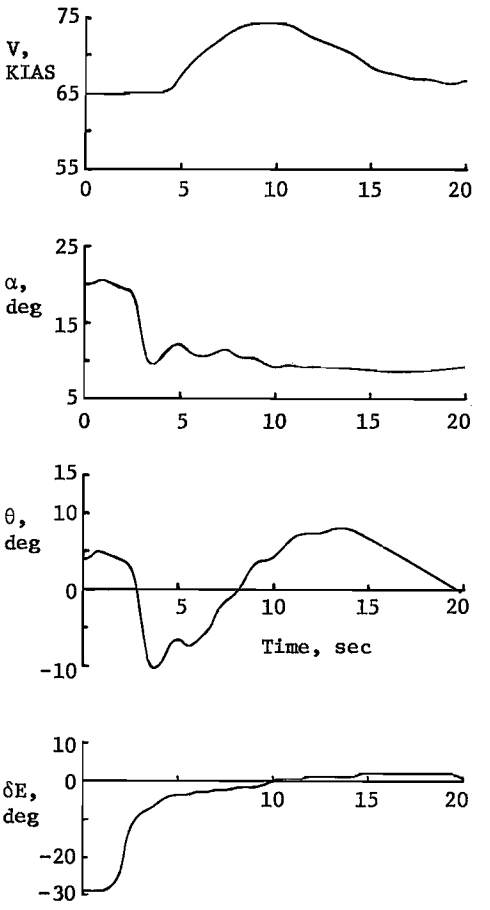

FIGURE 18. ARA Stall Recovery.

A well-damped short-period oscillation is evident in the α trace.

The ability to perform dynamic maneuvers in the stall region is of paramount importance for estimating nonlinear aerodynamic coefficients and damping parameters from flight data. Figure 19 demonstrates that the ARA's stall region can be traversed repeatedly using oscillating elevator inputs. A gradual power-off stalling maneuver was performed, and the phugoid mode was allowed to decay before the pilot began to oscillate the yoke between its aft limit and center position. The period of oscillation was close to the short period, and the ARA's response grew during the 10-sec interval shown here.

This run uncovered a need for extended sensor calibration and/or state estimation. The 5-KIAS peak-to-peak airspeed oscillation, which is in phase with the α and θ oscillations, is believed to result not from the aircraft's speed change but from wing wake effects on the static pressure port. Similarly, the short-period eigenvector magnitudes (Fig. 13b) imply that α and θ amplitudes should be very nearly equal, yet the θ oscillation is about a third larger than the α oscillation. The α-vane requires a rather significant upwash correction at low angles, which has been applied uniformly to the present data. There is reason to expect the upwash effect to decrease with increasing α. This and the α sensitivity of the airspeed

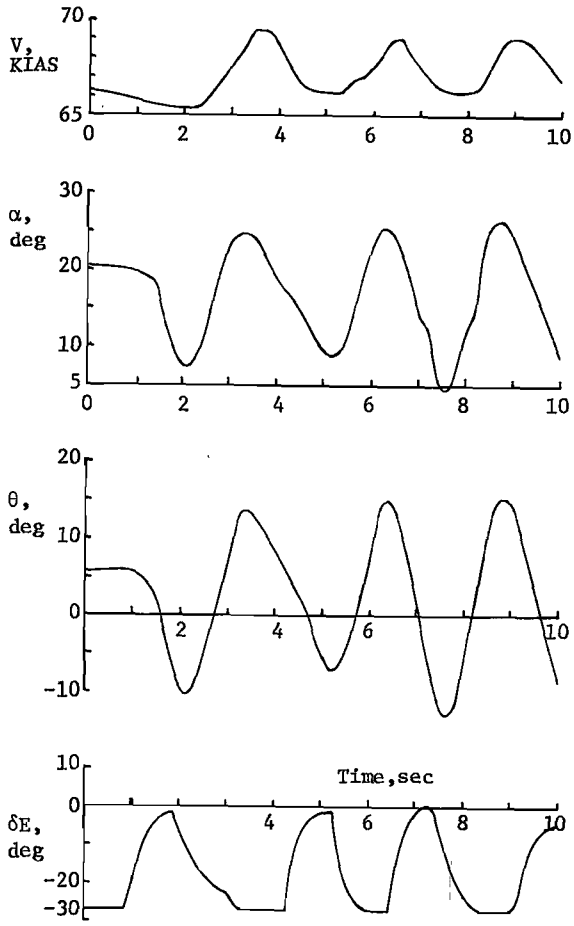

FIGURE 19. Effects of Elevator Pumping in the Stall.

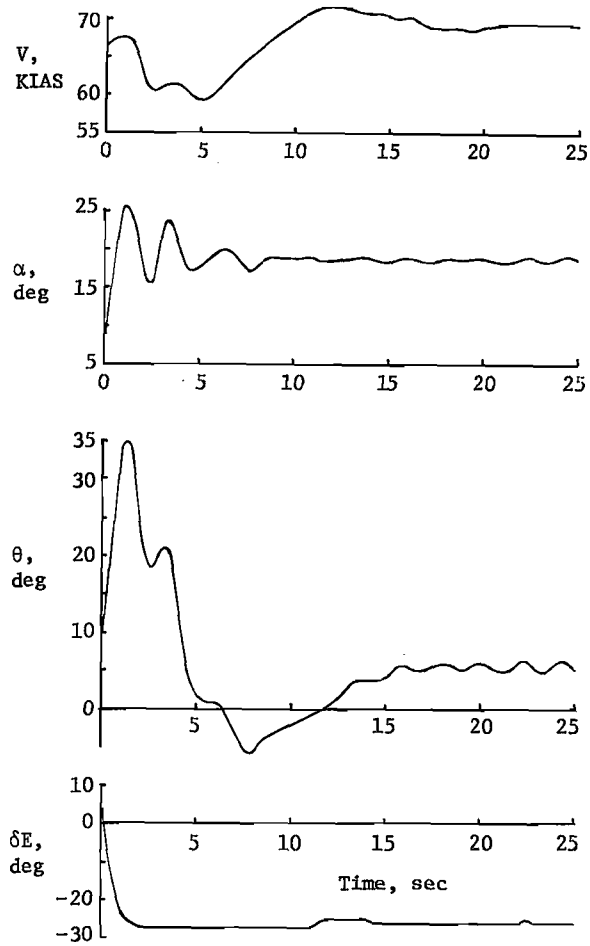

FIGURE 20. Abrupt ARA Stall. Starting Altitude = 2438 m(8000 ft).

measurement could be addressed by combining the present data with accelerometer measurements in an extended Kalman filter that includes sensor scale factors in an augmented state vector.

The aircraft could be stalled abruptly by swift aft motion of the yoke, as in Fig. 20. A lightly damped short period oscillation decreased frequency as the aircraft decelerated, and the θ response was strongly affected by the phugoid as well as the short period mode. The residual small-amplitude θ oscillation reflected effects of buffeting and the unplotted lateral-directional motions. There was direct evidence of pitch-roll coupling which remains to be analyzed.

Applying power during the stall decreased the gliding angle and decreased the airspeed, as predicted by Fig. 13c, and it made lateral-directional control more difficult. Figure 21 illustrates the effect of adding trim power 30 sec after the initiation of the abrupt stall shown in the previous figure. With increased elevator effect, α increased by about 3 deg, while θ increased more than 10 deg; consequently, the flight path was flattened. The rate of descent was cut in half, and the airspeed dropped.

Wing rock became a significant factor with power on: under conditions similar to those of Fig. 21, the roll oscillation could progress from 20° to over 60° amplitude in a single cycle. To identify longitudinal aerodynamic parameters in these circumstances, it will be necessary either to consider lateral-directional motions concurrently or to augment lateral-directional stability in the aircraft's flight control system.

Overall, the phenomena experienced in flight that were not adequately predicted from the combination of wind tunnel data and computer simulation were associated with the pitching stability of the aircraft, the buffeting encountered in the stall region, and, of course, the information regarding pilot opinion and technique. It is felt that the differences in static stability ultimately could be traced, but full-scale damping data presently can be obtained only in flight. Buffet levels could be measured in the tunnel, although allowance must be made for natural levels of turbulence in the wind tunnel. Pilot behavior and evaluation can be predicted from ground-based simulation, but validation of predictions can only be accomplished in actual flight.

CONCLUSIONS

A number of experimental and analytical methods have been used to investigate the stalling characteristics of a general aviation aircraft,

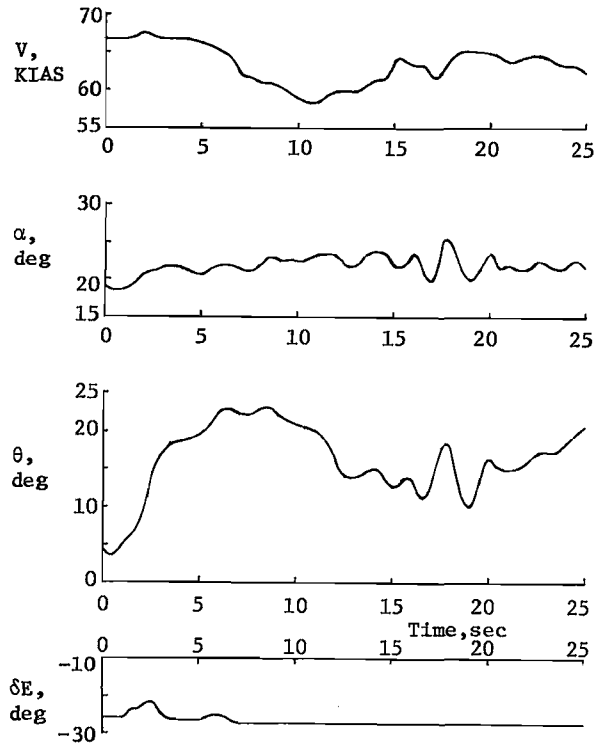

FIGURE 21. Effect of Adding Power During the Stall.

and several conclusions regarding testing and stall phenomena can be reached.

Full-scale wind tunnel data for the subject aircraft proved to be a valuable source of aerodynamic information, in that computed flight paths using these data were qualitatively similar to actual flight paths. The ability to portray power effects accurately was particularly significant. Considering the airspeed ranges of existing full-scale tunnels, they are well-suited to studying GA aircraft. For the future, it would be helpful to have data extending well beyond the stall and to investigate the effects of static aerodynamic coupling, buffet, and hysteresis.

Flight testing remains the only way to measure dynamic effects and to validate pilot behavior. The present flight tests have illustrated the capability to conduct research at high angle of attack, and they have indicated areas in which improved sensor calibration is required for accurate aerodynamic parameter identification. In particular, the α sensitivity of airspeed measurement and the flow distortion effects on α measurement must be addressed using state estimation or alternate data sources.

The importance of using trim data at various airspeeds, weights, and centers of gravity in defining the static nonlinear model should not be overlooked, as the data can be collected reliably, easily, and with few measurements over the aircraft's operating range up to stall. The ARA is well-behaved in power-off stall, and a limited amount of such data can be gathered during descent beyond the stall. More often than not, however, stalling flight is likely to involve continuing motions about all axes. Unless stability is augmented, lateral-directional effects must be considered in estimating longitudinal coefficients and vice-versa.

While stalling is an aerodynamic phenomenon, it is the ensuing motions and the pilot's response to them that are critical to safe flight. The aerodynamics, flight dynamics, and human interactions are inexorably coupled. By addressing the components as well as the whole, the current investigation seeks to reduce the threat to GA safety that is presented by the stall.

ACKNOWLEDGMENTS

This research was made possible by support from The Schultz Foundation of Clifton, New Jersey. Mr. George E. Miller provided flight test engineering support, and Mr. Gregory D. Hanson assisted in the flow visualization studies. Mr. Nixon performed the flight tests.

REFERENCES

1. Ellis, D., "A Study of Lightplane Stall Avoidance and Suppression", FAA-RD-77-25 (also Princeton University AMS Report No. 1320), Feb 1977.

2. --, "Special Study - Single-Engine, Fixed-Wing General Aviation Accidents", NTSB-AAS-79-1, May 1979.

3. Anderson, S., "Historical Overview of Stall/Spin Characteristics of General Aviation Aircraft", Journal of Aircraft, Vol. 16, No. 7, July 1979, pp. 455-461.

4. Hill, R., and Stevens, H., "Notes on Stalled Flying", ARC R&M No. 963, Oct 1922.

5. Jones, B., et al, "The Lateral Control of Stalled Aeroplanes. General Report by the Stability and Control Panel", ARC R&M No. 1000, Sept 1925.

6. Stevens, H., "The Behaviour of Certain Aeroplanes when the Controls are Abandoned in Stalled Flight", ARC R&M No. 1020, Nov 1925.

7. Gates, S., "Notes on Longitudinal Stability at Stalling in Gliding Flight", ARC R&M No. 1189, July 1928.

8. Garner, H., and Wright, K., "The Longitudinal Control of an Aeroplane Beyond the Stall", ARC R&M No. 1193, May 1928.

9. Soulé, H., and Gough, M., "Some Aspects of the Stalling of Modern Low-Wing Monoplanes", NACA TN 645, April 1938.

10. Hancock, G., "Problems of Aircraft Behaviour at High Angles of Attack", AGARDograph 136, April 1969.

11. Seddon, J. (ed.), Fluid Dynamics of Aircraft Stalling, AGARD-CP-102, Nov 1972.

12. Crimi, P., "Dynamic Stall", AGARD-AG-172, Nov 1973.

13. Taylor, C. (ed.), Aircraft Stalling and Buffeting, AGARD-LS-74, Feb 1975.

14. Scher, S., "Post-Stall Gyrations and Their Study on a Digital Computer", AGARD Report 359, April 1961.

15. Westbrook, C., Stall/Post-Stall/Spin Symposium, Wright-Patterson AFB, Dec 1971.

16. Thomas, H., and Collingbourne, J., "Longitudinal Motions of Aircraft Involving High Angles of Attack", ARC R&M 3753, 1974.

17. Paterson, J., et al, "The Stall Characteristics of Large Transport Aircraft", in Ref. 15, pp. G-1 to G-61.

18. McIntosh, W., and Wimpress, J., "Prediction and Analysis of the Low Speed Stall Characteristics of the Boeing 747", in Ref. 13, pp. 3-1 to 3-21.

19. Gerlach, O., "Determination of Stability Derivative and Performance Characteristics from Dynamic Manoeuvres", in Flight Test Techniques, AGARD-CP-85, Feb 1972, pp. 16-1 to 16-23.

20. Wingrove, R., "Estimation of Longitudinal Aircraft Characteristics using Parameter Identification Techniques", in Proceedings of the 9th Annual Symposium of the Society of Flight Test Engineers, Oct 1978.

21. Maine, R., and Iliff, K., "A Fortran Program Determining Aircraft Stability and Control Derivatives from Flight Data", NASA TN D-7831, April 1975.

22. Hall, W., Jr., Gupta, N., and Tyler, J., Jr., "Model Structure Determination and Parameter Identification for Nonlinear Aerodynamic Flight Regimes", in Methods for Aircraft State and Parameter Identification, AGARD-CP-172, May 1975, pp. 21-1 to 21-21.

23. Stalford, H., "Application of the Estimation-Before-Modeling (EBM) System Identification Method to the High Angle of Attack/Sideslip Flight of the T-2C Jet Trainer Aircraft", NADC-76097-30, Nov 1979.

24. Suit, W., "Aerodynamic Parameters of the Navion Airplane Extracted from Flight Data", NASA TN D-6643, Mar 1972.

25. Shivers, J., Fink, M., and Ware, G., "Full-Scale Wind-Tunnel Investigation of the Static Longitudinal and Lateral Characteristics of a Light Single-Engine Low-Wing Airplane", NASA TN D-5857, June 1970.

26. Seckel, E., and Morris, J., "Full-Scale Wind Tunnel Tests of a Low-Wing, Single-Engine, Light Plane with Positive and Negative Propeller Thrust and Up and Down Flap Deflection", NASA CR-1783, Aug 1971.

27. Edwards, L., "Wind Tunnel and Drop Tank Test Studies of the Correlation Between Model and Airplane Flight Characteristics", Princeton Univ. Senior Independent Work Report, May 1980.

28. McCormick, B., Aerodynamics, Aeronautics, and Flight Mechanics, J. Wiley & Sons, New York, 1979.

29. Brogan, W., Modern Control Theory, Quantum Publishers, New York, 1974.

30. Stengel, R., "Equilibrium Response of Flight Control Systems", in Proceedings of the 1980 Joint Automatic Control Conference, Aug 1980.

31. Scheubel, F., "The Effect of Density Gradient on the Longitudinal Motion of an Aircraft", Luftfahrtforschung, Vol. 19, No. 4, 1942, pp. 132-136; R.T.P. Translation 1939.

32. Phillips, W., "Simulation Study of the Oscillatory Longitudinal Motion of an Airplane at the Stall", NASA TP-1242, Aug 1978.